First-principles treatments of electron transport properties for nanoscale junctions

Yoshitaka Fujimoto* and Kikuji Hirose
Department of Precision Science and Technology, Osaka University, Suita, Osaka 565-0871, Japan
(Received 5 November 2002; revised manuscript received 12 March 2003; published 13 May 2003)

We present an efficient and highly accurate calculation method to provide first-principles electronic structures, current flow under steady states, and electric conductance for a nanoscale junction attached to truly semi-infinite crystalline electrodes on both sides. This method is formulated by the real-space finite-difference approach within the framework of the density functional theory. In our formalism, a scattering wave function infinitely extending over the entire system can be determined by carrying out the wave-function matching based on a boundary-value problem near the boundaries of the transition region which intervenes between the two electrodes with bulklike potentials, and consequently, for each incident propagating wave, the scattering wave function is constructed from the Green's function matrix defined in the transition region and the ratio matrices whose matrix elements are the ratios of the bulk solutions on neighboring grid points in the respective electrodes. This scheme completely eliminates numerical instability caused by the appearance of exponentially growing and decaying evanescent waves. In order to demonstrate the general applicability of the method, the calculation of the conductance of a gold nanowire suspended between semi-infinite Au(100) electrodes is presented as an example. We find that the transition from a metallic conductance of the quantum unit $(2e^2/h)$ to an insulating one takes place as the nanowire is stretched.

DOI: 10.1103/PhysRevB.67.195315 PACS number(s): 73.40.−c, 72.10.−d, 71.15.−m, 71.15.Ap

I. INTRODUCTION

In the last decade, as the miniaturization of electronic devices proceeds, the field of nanotechnology has received great attention more and more, and in particular, electron transport properties for nanoscale structures have been investigated actively because they are of significant importance from both fundamental and practical points of view. Recently, the unique phenomena of ballistic electron transport through nanoscale junctions such as quantized conductance[1–3] and negative differential conductance[4–8] have been observed experimentally and theoretically. In this situation, future researches on transport properties can be expected to lead to new discoveries of nano science and novel fabrications of electronic devices.

In order to obtain an exact theoretical knowledge on electron transport properties, we have to deal with a system of the nanoscale junction in contact with two truly *semi-infinite crystalline* electrodes (or leads); thereby an electron wave function extending over the entire system can be correctly described as a scattering state disturbed by the existence of the junction when an electron comes from infinitely deep inside of the crystalline electrode. The first problem to be encountered in this scheme is that the system inherently loses its periodic structure in the direction parallel to the junction. For such a system, a repeated slab model used in the conventional plane-wave expansion approach breaks down due to the difficulty of incorporating nonperiodicity in it. The next problem is that global wave functions for *infinitely* extended states continuing from one side to the other need to be accurately calculated.

The easiest way to treat this infinite system is to replace the semi-infinite crystalline electrode by a uniformly distributed charge background, i.e., "jellium."[5,7–12] However, this may give rise to a serious problem in evaluating electron transport properties, because there is an artificial interface between the fictitious potential of the structureless jellium electrode and the real potential of the crystal surface.

Up to now, there have been several attempts to treat genuine semi-infinite crystalline electrodes without the approximation of jellium. Most of these relied on a recursive calculation method from one side to the other, such as transfer- (or propagation-) matrix methods.[13–21] It is known, however, that when such recursive calculation techniques are employed as means of numerically solving the Kohn-Sham equation, numerical errors frequently accumulate exponentially in the matrix elements of the recursively multiplicated transfer matrix. This unfavorable situation is attributed to the appearance of exponentially growing and decaying waves, i.e., so-called evanescent waves.[12,22–27] In order to avoid this error accumulation, Wachutka proposed a way to improve the transfer-matrix methods by introducing a mathematical trick:[22] The main difference from the original transfer-matrix methods is that the wave-function matching scheme is based on a boundary-value problem instead of an initial-value problem in the transfer-matrix approaches.[22–27] However, Wachutka's prescription does not always work well. Indeed, the inherent instability in numerical calculations arises again when one attempts to include more intensively growing and decaying evanescent waves so as to describe the wave function more accurately.

In this paper, we present an efficient and highly accurate computational procedure for the first-principles theory of the nanoscale junction sandwiched by semi-infinite crystalline electrodes to overcome the above-mentioned numerical difficulties completely. Our procedure is formulated by the real-space finite-difference approach[28–32] within the framework of the density functional theory;[33,34] thereby the wave-function matching scheme is simply described and its implementation is easily performed. Our method accords with Wachutka's idea of treating the wave-function matching as a boundary-value problem; however, numerical errors can be

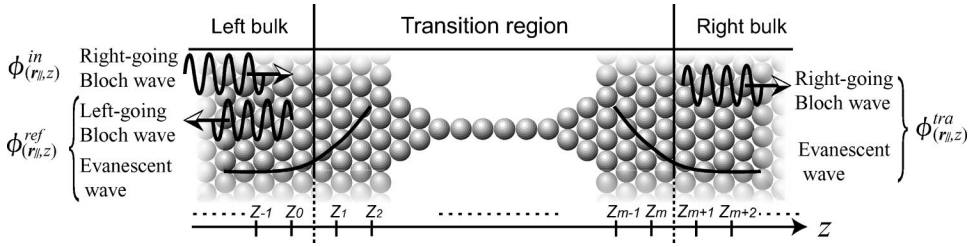

FIG. 1. Schematic representation of the system with the transition region intervening between the left and right semi-infinite crystalline bulks. $\boldsymbol{r}_{||}=(x,y)$ and z are coordinates perpendicular and parallel to the nanoscale junction, respectively. In the left bulk, the incident wave and the reflected waves including evanescent ones are represented as $\phi^{in}(\boldsymbol{r}_{||},z)$ and $\phi^{ref}(\boldsymbol{r}_{||},z)$, respectively, and in the right bulk, the propagating and decaying evanescent waves toward the right side are denoted by transmitted waves $\phi^{tra}(\boldsymbol{r}_{||},z)$.

completely eliminated, since evanescent waves are treated as the *ratios* of their values at two neighboring grid points in the discretized space. These ratios, which are mathematically equivalent to logarithmic derivatives, guarantee the numerical stability. The potential power of our procedure will be exhibited when it is applied to highly accurate calculations.

To exemplify the advantages of our technique, we apply it to investigating electron transport properties of a single-row gold nanowire suspended between Au(100) electrodes. We find that the electric conductance of the nanowire with three atoms is close to the quantum unit G_0 ($G_0=2e^2/h$, e: the electron charge, h: Planck's constant) when its average interatomic distance is less than 6.32 a.u., and decreases rapidly to zero as the nanowire is further stretched.

Our formalism can include the norm-conserving pseudopotential techniques;[35–38] however, throughout this paper we restrict ourselves to the case of the *local* pseudopotentials, in order to describe the essence of our procedure for avoiding numerical instability. The inclusion of nonlocal parts of the norm-conserving pseudopotentials is straightforward, which will be discussed in a forthcoming paper.

The plan of this paper is as follows. In Sec. II, we give in detail the first-principles computation scheme for the electronic structures and transport properties of the system with the junction between truly semi-infinite crystalline electrodes. In Sec. III, in order to demonstrate the general applicability of the method, the calculation of the conductance of the gold nanowire under elongation is presented as an example. In Sec. IV, we summarize our procedures. Finally, mathematical details are described in some appendixes.

II. THEORETICAL FORMALISM

We consider the procedure for obtaining the solutions of the Kohn-Sham equation in a system with the transition region intervening between two semi-infinite crystalline bulks, as depicted in Fig. 1. The transition region is representative of a nanoscale junction, a tunnel junction in tip-sample system (e.g., scanning tunneling microscopy), an interface between different bulks, an interstitial lattice defect or disorder, and so on. In general, an effective potential is close to periodic bulk potentials as goes deeply inside the left and right bulks. This fact allows us to make an approximation that the entire system can be divided into three parts: the left bulk, the transition region, and the right bulk (Fig. 1). The transition region should be large enough that the potential on the boundary planes in the transition region can be sufficiently smoothly connected with the periodic potentials of the respective bulks.

The global solutions of the Kohn-Sham equation extending over the entire system are constructed from a linear combination of partial solutions within the left and right bulks. More concretely, the solution we wish to calculate is a scattering wave function specified by a particular incident Bloch wave, e.g., an incident wave $\phi^{in}(\boldsymbol{r}_{||},z)$ incoming from deep inside the left bulk, as illustrated in Fig. 1. Here, $\boldsymbol{r}_{||}=(x,y)$ and z are coordinates perpendicular and parallel to the nanoscale junction, respectively, and two-dimensional periodicity is assumed for the $\boldsymbol{r}_{||}$ coordinates and nonperiodicity for the z one. The asymptotic form of the scattering wave function consists of the incident wave $\phi^{in}(\boldsymbol{r}_{||},z)$ plus reflected waves $\phi^{ref}(\boldsymbol{r}_{||},z)$ in the left bulk and transmitted waves $\phi^{tra}(\boldsymbol{r}_{||},z)$ in the right bulk. Then, we will construct the global scattering wave function satisfying this asymptotic behavior by means of matching together the near-boundary values of the wave function, i.e., its values near the right boundary of the left bulk and those near the left boundary of the right bulk, overbridging the transition region. Thus our wave-function matching procedure is referred to as the *overbridging boundary-matching* method. For this purpose, we will define a Green's function matrix in the transition region.

Our theoretical formalism relies upon the real-space finite-difference approach. This approach, which is summarized in Appendix A, enables us to derive readily the overbridging boundary-matching formula without introducing any complexity. The derivation of the matching formula will be demonstrated in Sec. II A. For the construction of the generalized Bloch functions, i.e., the solutions of the Kohn-Sham equation inside the bulk regions $\phi^{A}(\boldsymbol{r}_{||},z)(A=in,ref,$ and $tra)$, we propose two methods: one is the method of working out a generalized eigenvalue problem under the generalized Bloch theorem, and the other is to treat the ratios of the values of the bulk solutions at adjacent z_k grid points in a continued-fraction form. We will show that for the implementation of the overbridging boundary-matching formula, both methods are required to be employed together. The formulation of these two methods will be exhibited in Sec. II B.

A. Overbridging boundary-matching method

In this subsection, we give a wave-function matching procedure to construct the global wave function extending over

the entire system, based on the real-space finite-difference approach. As shown in Appendix A, a columnar vector $\Psi(z_k)$ consisting of N_{xy} $(=N_x \times N_y)$ values of the wave function on the x-y plane at the $z=z_k$ point satisfies the discretized Kohn-Sham equation (A5) that takes a simple form in the relation of three adjacent terms along the z direction in the case of the central finite difference, where N_x and N_y are the numbers of grid points in the x and y directions, respectively. In this paper we limit our formulation to the case of the central finite difference for simplicity. The extension of the methodology to the case of higher-order finite difference is straightforward. Because the Kohn-Sham equation is a second-order differential equation, the solution is determined by specifying the values $\Psi(z_k)$ at two different z_k points.[39] As these specified values, we choose $\Psi(z_{-1})$ and $\Psi(z_{m+2})$ outside the transition region (see Fig. 1). Then, Eqs. (A5) for the z_k grid points from $k=0$ to $m+1$ are treated as a simultaneous linear equation with regard to $\{\Psi(z_0),\Psi(z_1),\ldots,\Psi(z_{m+1})\}$ for given values of $\Psi(z_{-1})$ and $\Psi(z_{m+2})$,

$$(E-\hat{H})\begin{bmatrix}\Psi(z_0)\\ \Psi(z_1)\\ \vdots\\ \Psi(z_m)\\ \Psi(z_{m+1})\end{bmatrix}=\begin{bmatrix}B_z^{\dagger}\Psi(z_{-1})\\ 0\\ \vdots\\ 0\\ B_z\Psi(z_{m+2})\end{bmatrix}, \qquad (1)$$

where E is a Kohn-Sham energy and $\hat{H}$ is the Hamiltonian of a truncated part of the system sandwiched between the planes at $z=z_0$ and z_{m+1}, which is expressed by a block-tridiagonal matrix

$$\hat{H}=\begin{bmatrix}V(z_0) & B_z & & & 0\\ B_z^{\dagger} & V(z_1) & B_z & & \\ & \ddots & \ddots & \ddots & \\ & & B_z^{\dagger} & V(z_m) & B_z\\ 0 & & & B_z^{\dagger} & V(z_{m+1})\end{bmatrix}. \qquad (2)$$

Here the block matrices B_z and $V(z_k)$ are defined by Eqs. (A6) and (A7), respectively. Thus, once the Green's function matrix $\hat{G}=(E-\hat{H})^{-1}$ at a given energy E and lateral wave vector $\boldsymbol{k}_{||}$ is known, Eq. (1) is solved as

$$\begin{bmatrix}\Psi(z_0)\\ \Psi(z_1)\\ \vdots\\ \Psi(z_m)\\ \Psi(z_{m+1})\end{bmatrix}=\hat{G}\begin{bmatrix}B_z^{\dagger}\Psi(z_{-1})\\ 0\\ \vdots\\ 0\\ B_z\Psi(z_{m+2})\end{bmatrix}. \qquad (3)$$

From Eq. (3), one can see that all the values of the wave function in the transition region, $\Psi(z_1)$, $\Psi(z_2)$, . . . , and $\Psi(z_m)$, are directly connected to the two values of $\Psi(z_{-1})$ and $\Psi(z_{m+2})$ by means of the matrix $\hat{G}$, and further $\Psi(z_0)$ and $\Psi(z_{m+1})$ are related to $\Psi(z_{-1})$ and $\Psi(z_{m+2})$ as

$$\begin{bmatrix}\Psi(z_0)\\ \Psi(z_{m+1})\end{bmatrix}=\begin{bmatrix}G_{1,1} & G_{1,m+2}\\ G_{m+2,1} & G_{m+2,m+2}\end{bmatrix}\begin{bmatrix}B_z^{\dagger}\Psi(z_{-1})\\ B_z\Psi(z_{m+2})\end{bmatrix}, \qquad (4)$$

where $G_{i,j}$ is the N_{xy}-dimensional (i,j) block-matrix element of the Green's function matrix $\hat{G}$. Equation (4) is a realization of our overbridging boundary-matching formula to connect the values near the boundary of the left bulk, $\Psi(z_0)$ and $\Psi(z_{-1})$, and those of the right bulk, $\Psi(z_{m+1})$ and $\Psi(z_{m+2})$, where the near-boundary values of the wave function in the left and right bulks are directly connected with each other by the Green's function matrix carrying all of the information on the transition region.

Due to the screening effect in the semi-infinite crystalline bulks, the effective potential tends to take a periodic property deep inside the left and right bulks. For this reason, the appropriate way to construct the global scattering wave function for the entire system is to describe it in terms of a linear combination of generalized Bloch functions inside the left and right bulks (see later for the calculation of generalized Bloch functions in the bulks). The scattering wave function is classified into two types. One is incident from the left bulk with the reflection to the left bulk and transmission to the right bulk. The other solution is vice versa, i.e., incident from the right bulk with the reflection to the right bulk and transmission to the left bulk. Here, we consider only the solution in the former case. The solution in the latter case is constructed straightforwardly. As illustrated in Fig. 1, $\phi^{in}(\boldsymbol{r}_{||},z)$ is an incident Bloch wave coming from deep inside the left bulk, while $\phi^{ref}(\boldsymbol{r}_{||},z)$ is a set of reflected waves that propagate and decay into the left bulk. In the left-bulk region, the scattering wave function $\Psi(z_k)$ is expressed as a linear combination of these waves,

$$\Psi(z_k)=\Phi^{in}(z_k)+\sum_{l=1}^{N_{xy}} r_l\Phi_l^{ref}(z_k), \qquad (5)$$

where $r_l(l=1,\ldots,N_{xy})$ are reflection coefficients, and $\Phi_l^A(z_k)(A=in$ and $ref)$ are N_{xy}-dimensional columnar vectors constructed by $\{\phi^A(x_i,y_j,z_k):i=1\sim N_x,\ j=1\sim N_y\}$ on the plane at the z_k point in the left-bulk region. On the other hand, the scattering wave function $\Psi(z_k)$ in the right-bulk region is given by a linear combination of transmitted waves $\phi^{tra}(\boldsymbol{r}_{||},z)$ that propagate and decay into the right bulk with transmission coefficients t_l,

$$\Psi(z_k)=\sum_{l=1}^{N_{xy}} t_l\Phi_l^{tra}(z_k), \qquad (6)$$

where the columnar vector $\Phi_l^{tra}(z_k)$ at the z_k point in the right-bulk region has the N_{xy} components of $\{\phi^{tra}(x_i,y_j,z_k):i=1\sim N_x,\ j=1\sim N_y\}$. Thus, substituting Eqs. (5) and (6) into Eq. (4), we could determine all of the coefficients r_l and t_l in principle, if the generalized Bloch states Φ were known. However, Φ in this matching formula always include exponentially growing and decaying evanescent waves, and the inclusion of these evanescent waves inevitably gives rise to such a numerical problem that the smaller the grid spacing $h_i(i=x,y)$, the more serious the numerical errors. In the next Sec. III B 1, we will derive a

formula to calculate the generalized Bloch states Φ and discuss the applicability limitations of the formula. Eventually, the direct use of Eqs. (4)–(6) leads us to a numerical problem when calculations with a high degree of accuracy are demanded.

In order to circumvent this numerical difficulty, we introduce the following ratios of the generalized Bloch functions:

$$R^{ref}(z_0)=Q^{ref}(z_{-1})Q^{ref}(z_0)^{-1} \tag{7}$$

and

$$R^{tra}(z_{m+2})=Q^{tra}(z_{m+2})Q^{tra}(z_{m+1})^{-1}, \tag{8}$$

where $Q^A(z_k)(A=ref$ and $tra)$ are N_{xy}-dimesional matrices which gather generalized Bloch states $\Phi_l^A(z_k)$, i.e., $Q^A(z_k)=[\Phi_1^A(z_k),\ldots,\Phi_{N_{xy}}^A(z_k)]$. The ratio matrices $R^{ref}(z_0)$ and $R^{tra}(z_{m+2})$ do not involve the values of evanescent wave functions themselves, but include the *ratios* of the values of evanescent wave functions on the planes at two adjacent z points, which correspond to logarithmic derivatives in the continuous limit of real space,[25] and thus the numerical errors due to the appearance of evanescent waves never accumulate during computing the ratio matrices $R^{ref}(z_0)$ and $R^{tra}(z_{m+2})$. The method of directly calculating the ratio matrices, not *via* the values of evanescent wave functions themselves, will be shown in Sec. III B 2.

From Eqs. (5) and (7), we have

$$\Psi(z_0)=\Phi^{in}(z_0)+R^{ref}(z_0)^{-1}[\Psi(z_{-1})-\Phi^{in}(z_{-1})], \tag{9}$$

and similarly from Eqs. (6) and (8), we obtain

$$\Psi(z_{m+1})=R^{tra}(z_{m+2})^{-1}\Psi(z_{m+2}). \tag{10}$$

Then, inserting Eqs. (9) and (10) into Eq. (4), the wave-function matching formula (4) is rewritten in terms of the ratio matrices as

$$\begin{bmatrix} G_{1,1}B_z^\dagger-R^{ref}(z_0)^{-1} & G_{1,m+2}B_z \\ G_{m+2,1}B_z^\dagger & G_{m+2,m+2}B_z-R^{tra}(z_{m+2})^{-1} \end{bmatrix} \times\begin{bmatrix} \Psi(z_{-1}) \\ \Psi(z_{m+2}) \end{bmatrix}=\begin{bmatrix} -R^{ref}(z_0)^{-1}\Phi^{in}(z_{-1})+\Phi^{in}(z_0) \\ 0 \end{bmatrix}. \tag{11}$$

This is the final form of our overbridging boundary-matching formula. Note that an incident wave Φ^{in} in the right-hand side of Eq. (11) includes only the propagating one, and thus no evanescent waves themselves come out in Eq. (11). Eventually, the numerical instability caused by exponentially growing or decaying evanescent waves can be completely excluded in Eq. (11). It is noticed that $\Psi(z_{-1})$ and $\Psi(z_{m+2})$ are solved as the solutions of Eq. (11) for each incident propagating wave Φ^{in}, and once they are obtained, all the values of the global wave function around the transition region, $\Psi(z_k)(k=0,\ldots,m+1)$, are determined from Eq. (3), in which only a part of the block-matrix elements of the Green's function matrix, $G_{i,j}$ $(i=1\sim m+2,j=1$ and $m+2)$, are needed.

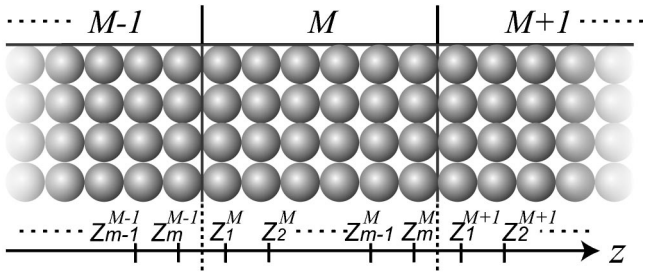

FIG. 2. Schematic representation of the periodic bulk. z_k^M represents the z coordinate at the kth discretized grid point in the Mth unit cell.

B. Computational scheme for generalized Bloch states in the crystalline bulk

We propose in this subsection two numerical methods to obtain the solutions of the Kohn-Sham equation in the bulk region, focusing on resolving numerical problems. One of the methods is to determine the generalized Bloch functions by means of solving a generalized eigenvalue equation. Using this method, we run up against a wall in numerical calculations when we attempt to acquire accurate evanescent wave functions, because there arises an inherent numerical problem that a great number of computational errors accumulate as the grid spacing h_x or h_y (see Appendix A) becomes small.[40] Nevertheless, the propagating Bloch waves and gently growing or decaying evanescent waves can be calculated with a high degree of accuracy. In other words, only the rapidly growing and decaying evanescent waves are smeared with serious numerical errors even when the calculation of the matrix elements of the generalized eigenvalue equation is satisfactorily carried out.

The other method is to treat the ratios of the generalized Bloch functions on the planes at two successive z points; thereby the numerical instability with respect to evanescent waves is completely prevented. In this method, the Kohn-Sham equation is rewritten in a continued-fraction form, and its solution is self-consistently determined so as to agree with the periodicity in the z direction. The *propagating* Bloch waves themselves, however, cannot be obtained by the continued-fraction method, and therefore we have to use these two methods in combination for the implementation of the overbridging boundary-matching formula (11).

1. Method of the generalized eigenvalue problem

The potential in the bulk region is periodic along the z direction (Fig. 2). Similarly to Eq. (1), the Kohn-Sham equation in the Mth unit cell is expressed as

$$(E-\hat{H}^M)\begin{bmatrix} \Phi(z_1^M) \\ \Phi(z_2^M) \\ \vdots \\ \Phi(z_{m-1}^M) \\ \Phi(z_m^M) \end{bmatrix}=\begin{bmatrix} B_z^\dagger\Phi(z_m^{M-1}) \\ 0 \\ \vdots \\ 0 \\ B_z\Phi(z_1^{M+1}) \end{bmatrix}. \tag{12}$$

Here, $\hat{H}^M$ is the Hamiltonian in the Mth unit cell regarded as an isolated system,

$$\hat{H}^M=\begin{bmatrix} V(z_1^M) & B_z & & & 0 \\ B_z^\dagger & V(z_2^M) & B_z & & \\ & \ddots & \ddots & \ddots & \\ & & B_z^\dagger & V(z_{m-1}^M) & B_z \\ 0 & & & B_z^\dagger & V(z_m^M) \end{bmatrix}, \tag{13}$$

where $V(z_k^M)$ is similar to Eq. (A7), representing the bulklike potential on the x-y plane at the z_k^M point. The wave function in the Mth unit cell is obtained by solving Eq. (12) as

$$\begin{bmatrix} \Phi(z_1^M) \\ \Phi(z_2^M) \\ \vdots \\ \Phi(z_{m-1}^M) \\ \Phi(z_m^M) \end{bmatrix} = \hat{G}^M \begin{bmatrix} B_z^\dagger \Phi(z_m^{M-1}) \\ 0 \\ \vdots \\ 0 \\ B_z \Phi(z_1^{M+1}) \end{bmatrix}, \tag{14}$$

where $\hat{G}^M$ is the Green's function matrix of the Hamiltonian $\hat{H}^M$:

$$\hat{G}^M=(E-\hat{H}^M)^{-1}. \tag{15}$$

The boundary values $\Phi(z_m^{M-1})$, $\Phi(z_1^M)$, $\Phi(z_m^M)$, and $\Phi(z_1^{M+1})$ are now related to each other,

$$\begin{bmatrix} \Phi(z_1^M) \\ \Phi(z_m^M) \end{bmatrix} = \begin{bmatrix} G_{1,1}^M & G_{1,m}^M \\ G_{m,1}^M & G_{m,m}^M \end{bmatrix} \begin{bmatrix} B_z^\dagger \Phi(z_m^{M-1}) \\ B_z \Phi(z_1^{M+1}) \end{bmatrix}, \tag{16}$$

where $G_{i,j}^M$ is the N_{xy}-dimensional (i,j) block-matrix element of the matrix $\hat{G}^M$.

Because of the periodicity along the z direction, the wave function satisfies the generalized Bloch condition

$$\Phi(z+L_z)=\lambda\Phi(z), \tag{17}$$

where $\lambda=e^{ik_zL_z}$, and k_z and L_z are a Bloch wave-vector component and unit-cell length in the z direction, respectively. In general, k_z is a complex number. According to condition (17), the relations between the values of the wave function at the z_m^M, z_1^{M+1} points and those at the z_m^{M-1}, z_1^M points are given by

$$\begin{bmatrix} \Phi(z_m^M) \\ \Phi(z_1^{M+1}) \end{bmatrix} = \lambda \begin{bmatrix} \Phi(z_m^{M-1}) \\ \Phi(z_1^M) \end{bmatrix}. \tag{18}$$

Thus, the insertion of Eq. (16) into Eq. (18) leads to a $2N_{xy}$-dimensional generalized eigenvalue equation[41]

$$\Pi_1 \begin{bmatrix} \Phi(z_m^{M-1}) \\ \Phi(z_1^{M+1}) \end{bmatrix} = \lambda \Pi_2 \begin{bmatrix} \Phi(z_m^{M-1}) \\ \Phi(z_1^{M+1}) \end{bmatrix}, \tag{19}$$

where

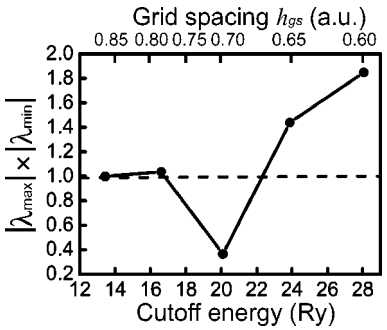

FIG. 3. Multiplication of the maximum and minimum absolute values of the eigenvalues as a function of the cutoff energy or the grid spacing h_{gs} $(=h_x=h_y=h_z)$ in the case of the Au bulk with $6s$ electrons.

$$\Pi_1=\begin{bmatrix} G_{m,1}^M B_z^\dagger & G_{m,m}^M B_z \\ 0 & I \end{bmatrix},$$

$$\Pi_2=\begin{bmatrix} I & 0 \\ G_{1,1}^M B_z^\dagger & G_{1,m}^M B_z \end{bmatrix}. \tag{20}$$

The eigenstates are classified into two classes depending on the absolute values of the eigenvalues λ: the eigenstates with $|\lambda|=1$ represent propagating Bloch waves, and the k_z is a real number. In the case of $|\lambda|\neq 1$, they are evanescent waves, and k_z is extended to the field of a complex number. The apparent advantage of this method is the possibility that all of these generalized Bloch states at an assigned energy E and lateral Bloch phase $\boldsymbol{k}_{||}$ are simultaneously obtainable from Eq. (19). The generalized eigenvalue equation (19) can be numerically worked out by means of the QZ algorithm, one of standard solvers for a generalized eigenvalue problem. In order to demonstrate numerical accuracy of Eq. (19), we examined the eigenvalues calculated from Eq. (19). Figure 3 shows the multiplication of $|\lambda_{max}|$ by $|\lambda_{min}|$, which are computed numerically in double precision, where λ_{max} and λ_{min} are the eigenvalues with the maximum and minimum absolute values, respectively. It is known that if λ be an eigenvalue of Eq. (19), then λ^{*-1} is necessarily an eigenvalue of Eq. (19).[18,21] Hence, when λ_{max} and λ_{min} are *exact* eigenvalues of Eq. (19), the relation that $|\lambda_{max}|\times|\lambda_{min}|=1$ should be satisfied by them. Nevertheless, in Fig. 3 one finds that the calculated value of $|\lambda_{max}|\times|\lambda_{min}|$ is considerably away from 1 at a cutoff energy higher than $\sim$18 Ry, corresponding to a grid spacing smaller than $\sim$0.75 a.u.[42] The breaking of the relation $|\lambda_{max}|\times|\lambda_{min}|\neq 1$ means that eigenvalues, therefore eigenvectors as well, are smeared with numerical errors.

Consequently, we conclude for the numerical accuracy of the generalized eigenvalue equation (19) that (i) when a cutoff energy is chosen so high as to implement an accurate calculation, evanescent waves which rapidly grow or decay have serious numerical errors, and yet (ii) *accurate* solutions of both the propagating Bloch waves and the gently growing or decaying evanescent waves can always be obtained. The additional procedure for completely resolving the numerical

problem concerning rapidly varing evanescent waves will be shown in the next Sec. III B 2.

2. Continued-fraction method

An efficient and simple procedure to determine the ratios of the generalized Bloch functions on the planes at two neighboring z points is presented. We first treat the ratios of the generalized Bloch functions in the left bulk, R^{ref} of Eq. (7). As is evident from Eq. (A5), the N_{xy}-dimensional matrix $Q^{ref}(z_k^M)(=[\Phi_1^{ref}(z_k^M),\ldots,\Phi_{N_{xy}}^{ref}(z_k^M)])$ satisfies

$$-B_z^\dagger Q^{ref}(z_{k-1}^M)+A(z_k^M)Q^{ref}(z_k^M)-B_z Q^{ref}(z_{k+1}^M)=0, \tag{21}$$

where $A(z_k^M)=E-V(z_k^M)$. From Eq. (21), one can see that the ratio matrix on the neighboring z points,

$$R^{ref}(z_k^M)=Q^{ref}(z_{k-1}^M)Q^{ref}(z_k^M)^{-1}, \tag{22}$$

satisfies a two-term recursive matrix equation[12]

$$R^{ref}(z_{k+1}^M)=[A(z_k^M)-B_z^\dagger R^{ref}(z_k^M)]^{-1}B_z. \tag{23}$$

Then the successive use of Eq. (23) leads to a continued-fraction representation, which links $R^{ref}(z_k^{M+1})$ in the $(M+1)$th unit cell to $R^{ref}(z_k^M)$ in the Mth unit cell as

$$\begin{aligned}R^{ref}(z_1^{M+1})=&[A(z_m^M)-B_z^\dagger[A(z_{m-1}^M)-B_z^\dagger[\cdots-B_z^\dagger\\&\times[A(z_2^M)-B_z^\dagger[A(z_1^M)-B_z^\dagger R^{ref}(z_1^M)]^{-1}B_z]^{-1}\\&\times B_z\cdots]^{-1}B_z]^{-1}B_z]^{-1}B_z.\end{aligned} \tag{24}$$

We see that the calculation of Eq. (24) is a computationally hard task, since the successive operations of the inversion are demanded. In practice, instead of Eq. (24), we employ a more efficient formula in terms of the Green's function matrix elements, which is equivalent to Eq. (24) (see Appendix B1),

$$\begin{aligned}R^{ref}(z_1^{M+1})=&G_{m,m}^M B_z+G_{m,1}^M\\&\times B_z^\dagger[R^{ref}(z_1^M)^{-1}-G_{1,1}^M B_z^\dagger]^{-1}G_{1,m}^M B_z.\end{aligned} \tag{25}$$

On the other hand, along the same line as mentioned above, the ratio matrix R^{tra} of Eq. (8) in the right bulk can be shown to satisfy analogous equations to Eqs. (23)–(25) (see Appendix B 2).

Since the potential at the kth grid point in the $(M+1)$th unit cell is equal to that at the kth grid point in the Mth unit cell due to the periodicity, the generalized Bloch conditions imposed on the ratio matrices now read as (see Appendix B 3)

$$R^A(z_k^{M+1})=R^A(z_k^M)=R^A(z_k)(A=ref \quad \text{and} \quad tra). \tag{26}$$

The solutions $R^A(z_k)$ of the continued-fraction equations (25) and (B9) under constraints (26) can always be determined in a self-consistent manner. Indeed, we confirmed ourselves that when the crude solutions of Eq. (19) are chosen as initial guesses for $R^A(z_k)$, the correct solutions are immediately acquired by only several iterations of self-consistent cycles, surprisingly.

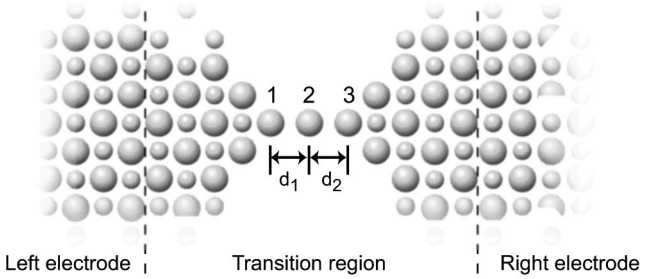

FIG. 4. Calculation model of the gold nanowire.

III. APPLICATION TO THE GOLD NANOWIRE

As an example of the method, we investigate the electric conductance of a single-row gold nanowire sandwiched by two semi-infinite crystalline gold electrodes when the nanowire is stretched. The gold nanowire system consists of a linear nanowire of three atoms labeled 1–3 and a pair of four-atom bases connected to both ends of the nanowire, and all of these are suspended between two semi-infinite Au(100) electrodes, as shown in Fig. 4. The transition region is chosen to be the area inside the dashed lines in Fig. 4, which includes the linear nanowire, the bases, and the respective three atomic layers of the left and right gold electrodes so that the potentials at both boundaries in the transition region can be smoothly connected to the bulklike potentials inside crystalline electrodes. The distance between the electrode and the basis as well as the distance between the left (right) basis and atom 1 (2) is set to be $0.5a_0$, which is equivalent to the length between two neighboring layers of the gold crystal in the [100] direction, where a_0 is the lattice constant of the gold crystal, i.e., $a_0=7.71$ a.u. The initial geometry in stretching the nanowire is chosen such that the interatomic distances d_1 and d_2 (see Fig. 4) are equal to the nearest-neighbor atomic distance in the gold crystal, 5.48 a.u. In our real-space finite-difference approach, the grid spacing h_{gs} $(=h_x=h_y=h_z)$ is taken to be 0.70 a.u., which corresponds to a cutoff energy of 20 Ry, and the second-order finite differentiation $(N_f=2)$ is adopted for the kinetic energy operator [see Eq. (A2)]. We use a unit cell with length of 15.4 a.u. in the x and y directions under periodic boundary conditions, accordingly the total number of grid points in these directions, $N_{xy}=22\times22$. Wave functions are calculated only at the Γ point in the two-dimensional Brillouin zone. The exchange-correlation effects are treated within the local density approximation parametrized by Perdew and Zunger.[43]

In the calculation of the conductance, we employ a local pseudopotential of the gold $6s$ electron described in Refs. 35 and 36, neglecting the contribution of the $5d$ electrons to the conductance, because the Au nanowires[10,44,45] as well as the Au bulk[25,46] exhibit the electronic structures mostly characterized by the $6s$ orbital at the Fermi level. The electronic structures of the bulk Au and the transition region are calculated self-consistently using standard supercell geometry

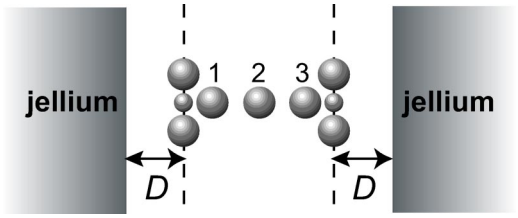

FIG. 5. Schematic representation of the nanowire attached to jellium electrodes. The length D represents the distance from the surface of the jellium to the square basis of the nanowire. Each atom of the nanowire is equally located with the interatomic distance of 5.48 a.u.

with the three-dimensional periodic boundary. Thus, the effective potential determined in this way is employed for the calculation of the conductance.

The values of the global scattering wave function near both boundaries of the transition region, $\Psi(z_{-1})$ and $\Psi(z_{m+2})$, are determined by the overbridging boundary-matching formula (11), and then the global wave functions extending over the entire system are calculated using Eq. (3). The bulk solutions and their ratios inside the left and right electrodes are acquired from Eqs. (19), (25), and (B9). Some remarks for obtaining the conductance within our method are given in Appendix C.

Some authors have reported theoretical studies on transport properties of nanowires sandwiched by two *jellium* electrodes instead of crystalline electrodes.[5,7–11] Owing to the existence of a possible artificial interface between the approximated constant potential of the jellium electrode and the real potential of the crystal surface, the problem may arise that the results for transport properties in the case of the jellium electrode are different from those in the case of the actual crystalline electrode. In practice, no one can know in advance such an appropriate distance D between the jellium electrode and the basis (see Fig. 5) that the correct conductance in the case of the crystalline electrode may be satisfactorily produced upon employing the jellium electrode. Before moving on to the discussion of transport properties in the case of the crystalline electrode, we briefly report the conductance of the gold nanowire suspended between two semi-infinite jellium electrodes for the various values of distance D. The electron density of the jellium electrode is taken equal to the average $6s$ valence-electron density of the gold crystal ($r_s=3.0$ a.u.).[7] In Fig. 6, the conductances calculated at the Fermi level are plotted as a function of D for the gold nanowire made of three atoms equispaced at 5.48 a.u. It can be seen that the conductances sensitively change depending on D, even though the geometrical structure of the nanowire is kept fixed. The distance $0.5a_0$ ($=3.85$ a.u.) indicated by the arrow in Fig. 6 corresponds to the length between two neighboring layers of the bulk Au in the [100] direction. The conductance at $D=0.5a_0$ is found to be $\sim 0.5G_0$. This value of the conductance should be compared with the true one at $D=0.5a_0$ and $d_1=d_2=5.48$ a.u. in the case of the crystalline electrode, $\sim 1.0G_0$, which will be shown later. Accordingly, in order to acquire a more correct value of the conductance upon employing the jellium electrode, we have to choose the distance D with prudence, e.g.,

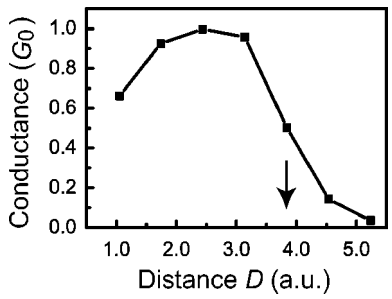

FIG. 6. Conductances of the gold nanowire sandwiched between the jellium electrodes as a function of the distance D between the basis and the surface of the semi-infinite jellium electrode. The gold nanowire is made of three atoms equispaced at 5.48 a.u. The arrow indicates $D=3.85$ a.u., which corresponds to the length between two neighboring layers of the bulk Au in the [100] direction.

in the present case $D\approx 2.5$ a.u.

We now turn to the discussion on atomic geometries and transport properties of the gold nanowire under elongation in the case of crystalline electrodes. First, we give in Fig. 7 the atomic structure optimized by the first-principles approach using the three-dimensional periodic supercell: the supercell with a length of 15.4 a.u. in the x and y directions containing

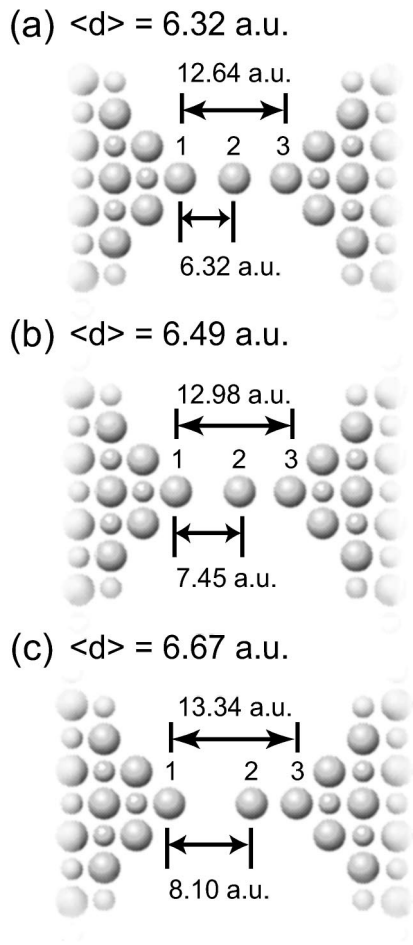

FIG. 7. Optimized geometries of the gold nanowire under elongation. $\langle d\rangle[=(d_1+d_2)/2]$ is the average interatomic distance.

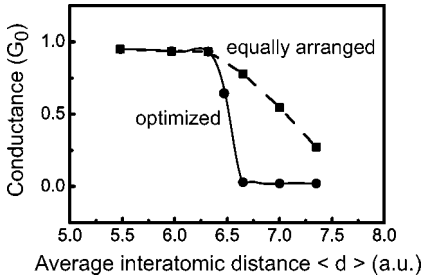

FIG. 8. Conductances of the three-gold-atom wire sandwiched between the Au(100) electrodes as a function of the average interatomic distance $\langle d \rangle$. The solid (dashed) curve denotes the conductance for the optimized (equally arranged) structure.

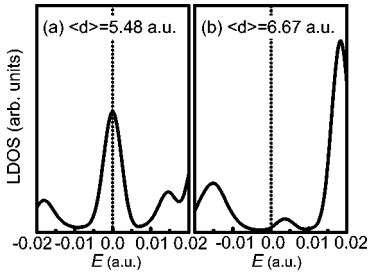

FIG. 9. LDOS of the 6*s* electron around the linear nanowire part for the optimized structures at $\langle d \rangle = (a)5.48$ and (b) 6.67 a.u. as a function of the incident electron energy E measured from the Fermi level. The zero of energy is chosen to be the Fermi level.

the linear nanowire, two bases, and one electrode with three atomic layers of the Au(100) surface. According to Ref. 10, the optimization of the atomic geometries was carried out under the restriction that both of the end atoms of the nanowire as well as the atoms of the bases and electrodes be kept frozen. Our first-principles molecular-dynamics (FPMD) simulations are based on the real-space finite-difference method employing the timesaving double-grid technique,[32] and the norm-conserving pseudopotentials of the gold 5*d* and 6*s* electrons are adopted.[37,38] We take a grid spacing of 0.33 a.u., corresponding to a cutoff energy of 90.9 Ry. As an initial configuration in FPMD simulations, the gold atoms in the nanowire are set at equal distances of 5.48 a.u., and then relieving the force acting on the central atom 2, we repetitiously elongate the electrode spacing. From Fig. 7(a) one finds that while the average interatomic distance $\langle d \rangle$ $[=(d_1+d_2)/2]$ is between 5.48 and 6.32 a.u., the three atoms of the nanowire keep equal spacings. When $\langle d \rangle$ is larger than 6.32 a.u., the interatomic distance dramatically changes, and the distance d_1 becomes large up to 8.10 a.u. at $\langle d \rangle = 6.67$ a.u., as illustrated in Fig. 7(c). This behavior is analogous to the result of Ref. 47 based on the FPMD simulation where near-central atoms of the nanowire also move toward one side of the electrodes in the process of the stretching.

Next, electron transport properties of the nanowire in the limit of zero bias are presented. Figure 8 shows the conductances at the Fermi level as a function of $\langle d \rangle$ for both the optimized and equally arranged structures of the gold nanowire with the three atoms. During the stretching from $\langle d \rangle = 5.48$ a.u. to 6.32 a.u., the conductances hardly change but keep a nearly quantized value of $1G_0$. Our result at $\langle d \rangle = 5.48$ a.u. is in agreement with the predictions of the tight-binding approach for the unstretched three-gold-atom wire.[44,48] When $\langle d \rangle$ becomes larger than about 6.32 a.u., the conductances in both the optimized and equally arranged cases decrease rapidly. In particular, the conductance in the optimized case diminishes more drastically and is close to zero at $\langle d \rangle = 6.67$ a.u. Thus one sees that a metal-insulator transition takes place in the three-gold-atom wire while the average interatomic distance $\langle d \rangle$ is from 6.32 a.u. to 6.67 a.u.

We show in Fig. 9 the local density of states (LDOS) of the 6*s* electron around the linear nanowire part for the optimized structures at $\langle d \rangle = 5.48$ and 6.67 a.u. as a function of the energy measured from the Fermi level. The LDOS is obtained by integrating the charge density at a given energy within a cylinder of radius 7.7 a.u. with ends 1.0 a.u. from the outermost atoms 1 and 3 in Fig. 4. The LDOS of $\langle d \rangle = 5.48$ a.u. has a distinct peak at the Fermi level, and this on-peak behavior of the LDOS implies the appearance of a fully opened channel at the Fermi level to yield the quantized conductance of $\sim 1G_0$.[8,11,45] On the other hand, the LDOS of $\langle d \rangle = 6.67$ a.u. exhibits off-peak behavior at the Fermi level, which gives rise to zero conductance.

Figure 10 illustrates the density distribution of the 6*s* electron incident from the left electrode at the Fermi level for the optimized structures at $\langle d \rangle = 5.48$ and 6.67 a.u. One can clearly recognize that the distribution at $\langle d \rangle = 5.48$ a.u. possesses a characteristic of the resonance state, i.e., an eigenmode pattern with a loop at the center of the nanowire. On the contrary, the distribution at $\langle d \rangle = 6.67$ a.u. shows a disappearance of the electron conductance, since electrons incoming from the left electrode are thoroughly scattered back around atom 1. Therefore, the bond of the nanowire is breaking at $\langle d \rangle = 6.67$ a.u.

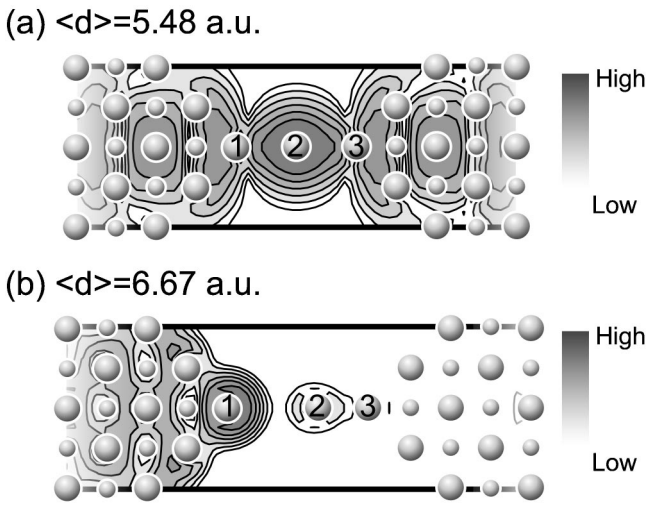

FIG. 10. Electron-density distribution at the Fermi level for the optimized structures at $\langle d \rangle = (a)5.48$ and (b) 6.67 a.u. The case of the incident 6*s* electron coming from the left electrode is considered. The planes shown are perpendicular to the [100] direction and contain the atoms in the nanowire.

IV. SUMMARY

We have presented new first-principles procedures to handle a system of the nanoscale junction attached to semi-infinite crystalline electrodes on both sides. Our method enables us to implement highly accurate calculations on the electronic structure and transport properties of almost any infinitely extending system without periodicity, such as a genuine surface, an interface, and a tip-sample system, as well as a nanoscale junction. The main points of the method are as follows: A global wave function extending over the entire system, being treated as a scattering wave function satisfying proper asymptotic conditions of scattering, is determined by matching together its near-boundary values outside the transition region intervening between two semi-infinite bulks, i.e., its values near the right boundary of the left bulk and those near the left boundary of the right bulk, by making use of the Green's function matrix carrying all of the information on the transition region. As a consequence, for each incident propagating wave, the global wave function is constructed from this Green's function matrix and the ratio matrices made of the generalized Bloch functions on neighboring grid points in the respective bulks. These ratio matrices are directly obtained by solving self-consistently the continued-fraction equations derived from the Kohn-Sham equation inside the periodic bulks. A sequence of the procedures completely excludes the computational errors caused by the appearance of exponentially growing and decreasing evanescent waves.

As an application, we have calculated electron transport properties of the three-gold-atom wire stretched between semi-infinite Au(100) electrodes. The transition from a metallic conductance of $\sim 1 G_0$ to an insulating one is observed when the average interatomic distance changes from 6.32 a.u. to 6.67 a.u.

By virtue of the simplicity of its scheme, our method can readily include norm-conserving pseudopotential techniques. We will discuss this developement in an extended paper later.

ACKNOWLEDGMENTS

This work was supported by a Grant-in-Aid for COE Research (No. 08CE2004) from the Ministry of Education, Culture, Sports, Science, and Technology of Japan, and one of authors (Y. F.) acknowledges financial support from a Grant-in-Aid for JSPS Fellows. The numerical calculations were carried out at Cyber media center of Osaka University and at the Institute for Solid State Physics at the University of Tokyo.

APPENDIX A: REPRESENTATION OF THE KOHN-SHAM EQUATION IN THE REAL-SPACE FINITE-DIFFERENCE APPROACH

The Kohn-Sham equation for the system depicted in Fig. 1 is written as

$$\left[-\frac{1}{2}\nabla^2+v_{eff}(\boldsymbol{r}_{||},z)\right]\psi(\boldsymbol{r}_{||},z)=E\psi(\boldsymbol{r}_{||},z) \quad (-\infty<z<\infty). \tag{A1}$$

The effective potential $v_{eff}(\boldsymbol{r}_{||},z)$ is described as a sum of local potentials $v_{ion}(\boldsymbol{r}_{||},z)$, the Hartree potential $v_H[\rho(\boldsymbol{r}_{||},z)]$, and the exchange-correlation potential $v_{xc}[\rho(\boldsymbol{r}_{||},z)]$ with the electronic charge denstiy $\rho(\boldsymbol{r}_{||},z)$. We use the atomic units $\hbar=e=m=1$ and assume two-dimensional periodicity for the $\boldsymbol{r}_{||}$ $[=(x,y)]$ coordinates and nonperiodicity for the z one.

In the real-space finite-difference approach, wave functions, electronic charge density, and potentials are directly represented on uniform three-dimensional real-space grids.[28–32] The x and y coordinates in the unit cell of periodicity are divided into grids $\{x_i;i=1,\ldots,N_x\}$ and $\{y_j;j=1,\ldots,N_y\}$ with equispacings h_x and h_y, respectively, while due to the nonperiodicity, the z axis is divided into grids $\{z_k;k=-\infty,\ldots,-1,0,1,\ldots,+\infty\}$ with an interval of h_z. Then, the Kohn-Sham equation (A1) is expressed within the real-space finite-difference approach as

$$\begin{aligned}-\frac{1}{2}\sum_{n=-N_f}^{N_f}&[c_x^n\psi(x_i+nh_x,y_j,z_k)+c_y^n\psi(x_i,y_j+nh_y,z_k)\\&+c_z^n\psi(x_i,y_j,z_k+nh_z)]+v_{eff}(x_i,y_j,z_k)\psi(x_i,y_j,z_k)\\&=E\psi(x_i,y_j,z_k),\end{aligned} \tag{A2}$$

where c_μ^n $(\mu=x,y,z)$ are constant parameters due to the finite differentiation of kinetic energy operator $-\frac{1}{2}\nabla^2$. For simplicity, we deal below with the simplest case of the central finite difference $(N_f=1)$ with the parameters $c_\mu^{-1}=c_\mu^1=1/h_\mu^2$ and $c_\mu^0=-2/h_\mu^2$ $(\mu=x,y,z)$. When higher-order finite-difference formulas are employed, see Ref. 29 for the values of c_μ^n. Owing to the periodicity of the x and y directions, the following Bloch conditions are imposed on the wave function: in the x direction

$$\psi(x_0,y_j,z_k)=e^{+ik_xL_x}\psi(x_{N_x},y_j,z_k), \tag{A3a}$$

$$\psi(x_{N_x+1},y_j,z_k)=e^{-ik_xL_x}\psi(x_1,y_j,z_k), \tag{A3b}$$

and in the y direction

$$\psi(x_i,y_0,z_k)=e^{+ik_yL_y}\psi(x_i,y_{N_y},z_k), \tag{A4a}$$

$$\psi(x_i,y_{N_y+1},z_k)=e^{-ik_yL_y}\psi(x_i,y_1,z_k), \tag{A4b}$$

where $e^{\pm ik_xL_x}$ $(e^{\pm ik_yL_y})$ represent the Bloch phase factors due to the periodicity of the $x(y)$ direction. $\boldsymbol{k}_{||}=(k_x,k_y)$ and (L_x,L_y) denote the two-dimensional vectors of Bloch wave numbers and lateral lengths of the unit cell, respectively.

It is convenient to treat a set of values of the wave function on the x-y plane at the $z=z_k$ point $\{\psi(x_i,y_j,z_k):i=1,\ldots,N_x,j=1,\ldots,N_y\}$ as a columnar vector $\Psi(z_k)$ of N_{xy} $(=N_x\times N_y)$ dimensions. Taking into account the Bloch conditions (A3) and (A4), we now rewrite Eq. (A2) in the case of the central finite difference as

$$-B_z^{\dagger}\Psi(z_{k-1})+[E-V(z_k)]\Psi(z_k)-B_z\Psi(z_{k+1})=0 \quad (k=-\infty,\ldots,-1,0,1,\ldots,\infty), \tag{A5}$$

where B_z is a constant matrix proportional to N_{xy}-dimensional unit matrix I,

$$B_z=-\frac{1}{2h_z^2}I, \tag{A6}$$

and $V(z_k)$ is the following N_{xy}-dimensional matrix defined on the x-y plane at the $z=z_k$ point:

$$V(z_k)=\begin{bmatrix} V_{z_k}(y_1) & B_y & 0 & & \cdots & & 0 & e^{ik_yL_y}B_y^{\dagger} \\ B_y^{\dagger} & V_{z_k}(y_2) & B_y & 0 & & \cdots & & 0 \\ 0 & \ddots & \ddots & \ddots & & & & \\ & & & \ddots & \ddots & \ddots & & \vdots \\ \vdots & & & & & & & \\ & & & & \ddots & \ddots & \ddots & 0 \\ 0 & & & \cdots & 0 & B_y^{\dagger} & V_{z_k}(y_{N_y-1}) & B_y \\ e^{-ik_yL_y}B_y & 0 & & \cdots & & 0 & B_y^{\dagger} & V_{z_k}(y_{N_y}) \end{bmatrix}, \tag{A7}$$

where B_y is an N_x-dimensional matrix similar to B_z,

$$B_y=-\frac{1}{2h_y^2}I, \tag{A8}$$

and the block matrix $V_{z_k}(y_j)$ is defined on the x line at the (y_i,z_k) point as

$$V_{z_k}(y_j)=\begin{bmatrix} v_{y_j,z_k}(x_1) & b_x & 0 & & \cdots & & 0 & e^{ik_xL_x}b_x \\ b_x & v_{y_j,z_k}(x_2) & b_x & 0 & & \cdots & & 0 \\ 0 & \ddots & \ddots & \ddots & & & & \\ & & & \ddots & \ddots & \ddots & & \vdots \\ \vdots & & & & & & & \\ & & & & \ddots & \ddots & \ddots & 0 \\ 0 & & & \cdots & 0 & b_x & v_{y_j,z_k}(x_{N_x-1}) & b_x \\ e^{-ik_xL_x}b_x & 0 & & \cdots & & 0 & b_x & v_{y_j,z_k}(x_{N_x}) \end{bmatrix}, \tag{A9}$$

$$b_x=-\frac{1}{2}c_x^1=-\frac{1}{2}c_x^{-1}=-\frac{1}{2h_x^2}, \tag{A10}$$

$$v_{y_j,z_k}(x_i)=\frac{1}{h_x^2}+\frac{1}{h_y^2}+\frac{1}{h_z^2}+v_{eff}(x_i,y_j,z_k). \tag{A11}$$

After all, it should be remarked that within the framework of the real-space finite-difference formalism, the discretized Kohn-Sham equation (A2) under the Bloch conditions (A3) and (A4) is rewritten as Eq. (A5) which is in a relation of three adjacent terms along the z direction.[49]

APPENDIX B: MATHEMATICAL DETAILS CONCERNING RATIO MATRICES

1. Proof for the validity of Eq. (25)

From Eq. (16), it is found that the sets of the generalized Bloch functions $Q^{ref}(z_1^M)$ and $Q^{ref}(z_m^M)$ link together with the other sets $Q^{ref}(z_m^{M-1})$ and $Q^{ref}(z_1^{M+1})$ as

$$Q^{ref}(z_1^M)=W_{1,1}^M Q^{ref}(z_m^{M-1})+W_{1,m}^M Q^{ref}(z_1^{M+1}), \tag{B1}$$

$$Q^{ref}(z_m^M)=W_{m,1}^M Q^{ref}(z_m^{M-1})+W_{m,m}^M Q^{ref}(z_1^{M+1}), \tag{B2}$$

where $W^M_{i,1}=G^M_{i,1}B^\dagger_z$ and $W^M_{i,m}=G^M_{i,m}B_z(i=1,m)$. Multiplication of $Q^{ref}(z^{M-1}_m)^{-1}$ from the right side of Eq. (B1) leads to

$$R^{ref}(z^M_1)^{-1}=W^M_{1,1}+W^M_{1,m}Q^{ref}(z^{M+1}_1)Q^{ref}(z^{M-1}_m)^{-1}, \tag{B3}$$

and similarly, Eq. (B2) multiplied by $Q^{ref}(z^{M+1}_1)^{-1}$ from the right side takes a form

$$R^{ref}(z^{M+1}_1)=W^M_{m,1}Q^{ref}(z^{M-1}_m)Q^{ref}(z^{M+1}_1)^{-1}+W^M_{m,m}. \tag{B4}$$

Rewriting Eq. (B3) as

$$Q^{ref}(z^{M-1}_m)Q^{ref}(z^{M+1}_1)^{-1}=[R^{ref}(z^M_1)^{-1}-W^M_{1,1}]^{-1}W^M_{1,m} \tag{B5}$$

and inserting Eq. (B5) into Eq. (B4), we have Eq. (25).

2. Equations for the ratio matrix R^{tra} to satisfy

The ratio matrix R^{tra} of Eq. (8) in the right bulk defined by

$$R^{tra}(z^M_k)=Q^{tra}(z^M_k)Q^{tra}(z^M_{k-1})^{-1} \tag{B6}$$

is found to obey a matrix equation

$$R^{tra}(z^M_k)=[A(z^M_k)-B_zR^{tra}(z^M_{k+1})]^{-1}B^\dagger_z \tag{B7}$$

and the corresponding continued-fraction equation

$$\begin{aligned}R^{tra}(z^N_1)=[A(z^M_1)-B_z[A(z^M_2)-B_z[\cdots-B_z[A(z^M_{m-1})\\ -B_z[A(z^M_m)-R^{tra}(z^{M+1}_1)]^{-1}B^\dagger_z]^{-1}B^\dagger_z\cdots]^{-1}\\ \times B^\dagger_z]^{-1}B^\dagger_z]^{-1}B^\dagger_z\end{aligned} \tag{B8}$$

and, further, a practically more useful form

$$\begin{aligned}R^{tra}(z^M_1)=G^M_{1,1}B^\dagger_z+G^M_{1,m}B_z[R^{tra}(z^{M+1}_1)^{-1}\\ -G^M_{m,m}B_z]^{-1}G^M_{m,1}B^\dagger_z.\end{aligned} \tag{B9}$$

3. Relation between the ratio matrices in successive unit cells

We show that the ratio matrix at the z^M_k in the Mth unit cell is equal to that at the same position z^{M+1}_k in the $(M+1)$th unit cell. The N_{xy}-dimensional matrix $Q(z^M_k)$ is defined by N_{xy} generalized Bloch states $\Phi_l(z^M_k)(l=1\sim N_{xy})$ as

$$Q(z^M_k)=[\Phi_1(z^M_k),\ldots,\Phi_{N_{xy}}(z^M_k)]. \tag{B10}$$

According to the generalized Bloch condition, $Q(z^{M+1}_k)$ in the $(M+1)$th unit cell is written as

$$Q(z^{M+1}_k)=[\lambda_1\Phi_1(z^M_k),\ldots,\lambda_{N_{xy}}\Phi_{N_{xy}}(z^M_k)], \tag{B11}$$

where λ_l is the lth generalized Bloch phase factor for the lth state. Therefore, we can derive the simple relation between $R(z^{M+1}_k)$ and $R(z^M_k)$ defined by Eq. (22) or (B6),

$$\begin{aligned}R(z^{M+1}_k)=Q(z^{M+1}_{k-1})Q(z^{M+1}_k)^{-1}=Q(z^M_{k-1})\begin{bmatrix}\lambda_1 & & 0\\ & \ddots & \\ 0 & & \lambda_n\end{bmatrix}\\ \times\begin{bmatrix}\lambda_1 & & 0\\ & \ddots & \\ 0 & & \lambda_n\end{bmatrix}^{-1}Q(z^M_k)^{-1}=R(z^M_k).\end{aligned} \tag{B12}$$

APPENDIX C: CALCULATION OF CONDUCTANCE

We here describe how the conductance is calculted in our formalism. The expression of the conductance G at the zero bias limit is simply given by the Landauer-Büttiker formula[50]

$$G=\frac{2e^2}{h}\sum_{i,j}|t_{ij}|^2\frac{v_i}{v_j}, \tag{C1}$$

where v_j and v_i are the z components of the expectation value of the velocity for the jth incident Bloch state Φ^{in}_j and that for the ith transmitted Bloch state Φ^{tra}_i, respectively,[51] and t_{ij} denotes the corresponding transmission coefficient. The procedure to calculate the transmission coefficients is shown below. In our formalism, the scattering wave function $\Psi_j(z_{m+2})=\Sigma_i t_{ij}\Phi^{tra}_i(z_{m+2})$ [see Eq. (6)] is directly determined by solving Eq. (11). Because the transition region is chosen large enough that the potential is effectively screened, $\Psi_j(z_{m+2})$ in the bulk region is actually constructed from only propagating Bloch waves with negligible contribution of evanescent waves. Therefore, the transmission coefficients t_{ij} are obtainable from the following equation for given values of $\Psi_j(z_{m+2})$ and transmitted *propagating* waves $\Phi^{tra}_i(z_{m+2})$:

$$\begin{aligned}\begin{bmatrix}\Phi^{tra^\dagger}_1\cdot\Phi^{tra}_1 & \cdots & \Phi^{tra^\dagger}_1\cdot\Phi^{tra}_{N_{tp}}\\ \vdots & & \vdots\\ \Phi^{tra^\dagger}_{N_{tp}}\cdot\Phi^{tra}_1 & \cdots & \Phi^{tra^\dagger}_{N_{tp}}\cdot\Phi^{tra}_{N_{tp}}\end{bmatrix}\begin{bmatrix}t_{1,j}\\ \vdots\\ t_{N_{tp},j}\end{bmatrix}\\ =\begin{bmatrix}\Phi^{tra^\dagger}_1\cdot\Psi_j\\ \vdots\\ \Phi^{tra^\dagger}_{N_{tp}}\cdot\Psi_j\end{bmatrix}.\end{aligned} \tag{C2}$$

Here, N_{tp} denotes the number of transmitted propagating waves and a dot $(\cdot)$ means the inner product. The summation in the inner product is taken over grid points within a unit cell on the x-y plane at $z=z_{m+2}$.

*Electronic address: fujimoto@cp.prec.eng.osaka-u.ac.jp

[1] S. Datta, *Electronic Transport in Mesoscopic Systems* (Cambridge University Press, New York, 1995); J. M. van Ruitenbeek, in *Metal Clusters at Surfaces Structure, Quantum Properties, Physical Chemistry*, edited by K. H. Meiwes-Broer (Springer, Berlin, 2000), and references therein.

[2] H. Ohnishi, Y. Kondo, and K. Takayanagi, Nature (London) **395**, 780 (1998).

[3] A. I. Yanson, G. R. Bollinger, H. E. van den Brom, N. Agrït, and J. M. van Ruitenbeek, Nature (London) **395**, 783 (1998).

[4] I.-W. Lyo and Ph. Avouris, Science (Washington, DC, U.S.) **245**, 1369 (1989).

[5] N. D. Lang, Phys. Rev. B **55**, 9364 (1997).

[6] J. Chen, M. A. Reed, A. M. Rawlett, and J. M. Tour, Science (Washington, DC, U.S.) **286**, 1550 (1999).

[7] M. Di Ventra, S.-G. Kim, S. T. Pantelides, and N. D. Lang, Phys. Rev. Lett. **86**, 288 (2001).

[8] S. Tsukamoto and K. Hirose, Phys. Rev. B **66**, 161402 (2002).

[9] José-Luis Mozos, C. C. Wan, G. Taraschi, J. Wang, and H. Guo, Phys. Rev. B **56**, R4351 (1997).

[10] M. Okamoto and K. Takayanagi, Phys. Rev. B **60**, 7808 (1999).

[11] N. Kobayashi, M. Aono, and M. Tsukada, Phys. Rev. B **64**, 121402 (2001).

[12] K. Hirose and M. Tsukada, Phys. Rev. Lett. **73**, 150 (1994); Phys. Rev. B **51**, 5278 (1995).

[13] P. M. Marcus and D. W. Jepsen, Phys. Rev. Lett. **20**, 925 (1968).

[14] D. W. Jepsen and P. M. Marcus, in *Computational Methods in Band Theory*, edited by P. M. Marcus, J. F. Janak, and A. R. Williams (Plenum, New York, 1971).

[15] J. A. Appelbaum and D. R. Hamann, Phys. Rev. B **6**, 2166 (1972).

[16] E. Foo, M. F. Thorpe, and D. Weaire, Surf. Sci. **57**, 323 (1976).

[17] E. J. Mele and J. D. Joannopoulos, Surf. Sci. **66**, 38 (1977); Phys. Rev. B **17**, 1816 (1978).

[18] D. H. Lee and J. D. Joannopoulos, Phys. Rev. B **23**, 4988 (1981); **23**, 4997 (1981).

[19] P. Sautet and C. Joachim, Phys. Rev. B **38**, 12 238 (1988).

[20] G. Taraschi, José-Luis Mozos, C. C. Wan, H. Guo, and J. Wang, Phys. Rev. B **58**, 13 138 (1998).

[21] D. Wortmann, H. Ishida, and S. Blügel, Phys. Rev. B **65**, 165103 (2002).

[22] G. Wachutka, Phys. Rev. B **34**, 8512 (1986).

[23] M. D. Stiles and D. R. Hamann, Phys. Rev. B **38**, 2021 (1988).

[24] W. Hummel and H. Bross, Phys. Rev. B **58**, 1620 (1998).

[25] K. Kobayashi, Phys. Rev. B **59**, 13 251 (1999).

[26] H. J. Choi and J. Ihm, Phys. Rev. B **59**, 2267 (1999).

[27] Y. Fujimoto and K. Hirose, Nanotechnology **14**, 147 (2003).

[28] J. R. Chelikowsky, N. Troullier, and Y. Saad, Phys. Rev. Lett. **72**, 1240 (1994).

[29] J. R. Chelikowsky, N. Troullier, K. Wu, and Y. Saad, Phys. Rev. B **50**, 11 355 (1994).

[30] X. Jing, N. Troullier, D. Dean, N. Binggeli, J. R. Chelikowsky, K. Wu, and Y. Saad, Phys. Rev. B **50**, 12 234 (1994).

[31] J. R. Chelikowsky, X. Jing, K. Wu, and Y. Saad, Phys. Rev. B **53**, 12 071 (1996).

[32] T. Ono and K. Hirose, Phys. Rev. Lett. **82**, 5016 (1999).

[33] P. Hohenberg and W. Kohn, Phys. Rev. **136**, B864 (1964).

[34] W. Kohn and L. J. Sham, Phys. Rev. **140**, A1133 (1965).

[35] D. R. Hamann, M. Schlüter, and C. Chiang, Phys. Rev. Lett. **43**, 1494 (1979).

[36] G. B. Bachelet, D. R. Hamann, and M. Schlüter, Phys. Rev. B **26**, 4199 (1982).

[37] N. Troullier and J. L. Martins, Phys. Rev. B **43**, 1993 (1991).

[38] K. Kobayashi, Comput. Mater. Sci. **14**, 72 (1999).

[39] The solution of a second-order differential equation can be determined by specifying a value and a first derivative at one point or by specifying values at two different points. We here adopt the latter.

[40] Taking a smaller $h_i (i=x,\ y)$, which corresponds to the inclusion of plane waves with a higher frequency in the lateral directions, gives rise to more rapidly growing and decaying evanescent waves.

[41] Analogous expressions of the generalized eigenvalue equation are found in Refs. 22–27.

[42] The cutoff energy is expressed by $(\pi/h_{gs})^2$ (Ry), where h_{gs} is the grid spacing (a.u.). See Ref. 32.

[43] J. P. Perdew and A. Zunger, Phys. Rev. B **23**, 5048 (1981).

[44] M. Brandbyge, N. Kobayashi, and M. Tsukada, Phys. Rev. B **60**, 17 064 (1999).

[45] S. Tsukamoto, T. Ono, Y. Fujimoto, K. Inagaki, H. Goto, and K. Hirose, Mater. Trans. **42**, 2257 (2001).

[46] N. V. Smith, Phys. Rev. B **9**, 1365 (1974).

[47] J. A. Torres, E. Tosatti, A. Dal Corso, F. Ercolessi, J. J. Kohanoff, F. D. Di Tolla, and J. M. Soler, Surf. Sci. **426**, L441 (1999).

[48] E. G. Emberly and G. Kirczenow, Phys. Rev. B **60**, 6028 (1999).

[49] The description of the Kohn-Sham equation in the relation of three adjacent terms is also possible in the Laue representation that employs a two-dimensional plane-wave expansion in the lateral directions and a real-space discretization for the z coordinate (e.g., see Ref. 12). The advantage of our real-space finite-difference method is that the finite differentiation for the kinetic operator is treated on the same footing in all the three directions.

[50] M. Büttiker, Y. Imry, R. Landauer, and S. Pinhas, Phys. Rev. B **31**, 6207 (1985).

[51] The method for calculating the component $v_k (k=i,j)$ is found in J. A. Appelbaum and E. I. Blount, Phys. Rev. B **8**, 483 (1973).